

NeuralPassthrough: Learned Real-Time View Synthesis for VR

Lei Xiao
Reality Labs Research, Meta
United States of America
lei.xiao@fb.com

Salah Nouri
Reality Labs Research, Meta
United States of America
snouri@fb.com

Joel Hegland
Reality Labs Research, Meta
United States of America
hegland@fb.com

Alberto Garcia Garcia
Reality Labs, Meta
Switzerland
agarcia@fb.com

Douglas Lanman
Reality Labs Research, Meta
United States of America
douglas.lanman@fb.com

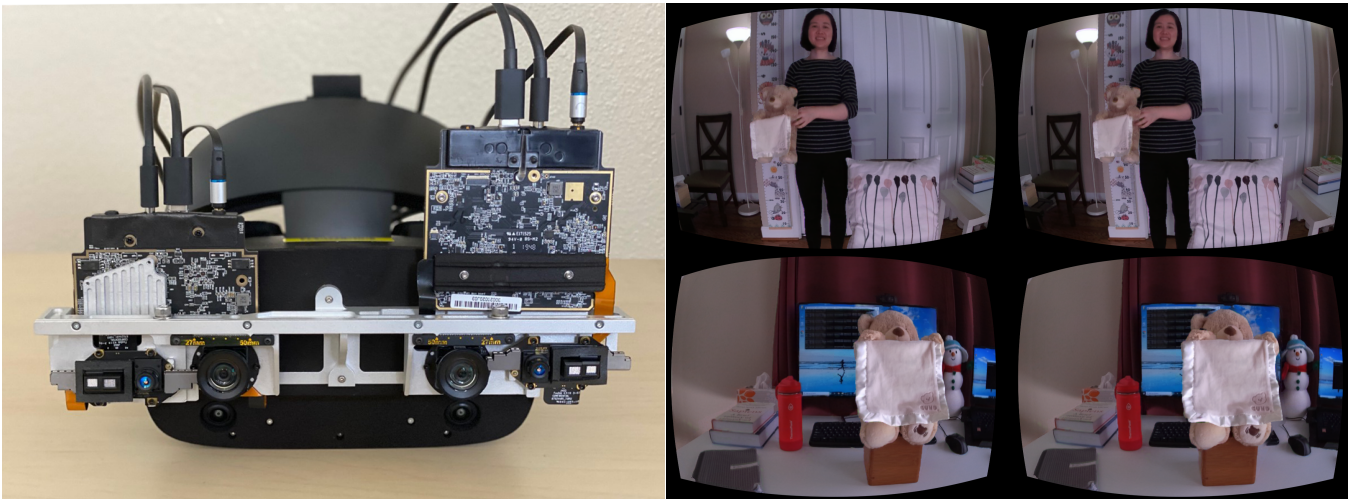


Figure 1: We demonstrate the first neural view synthesis method that is optimized to meet the unique requirements for VR passthrough, synthesizing perspective-correct viewpoints in real time and with high visual fidelity. *Left:* We demonstrate performance using a custom-built VR headset, containing a stereo RGB camera rig with an adjustable baseline. *Right:* Our method runs in real-time and supports dynamic scenes (top) and near-field objects (bottom).

ABSTRACT

Virtual reality (VR) headsets provide an immersive, stereoscopic visual experience, but at the cost of blocking users from directly observing their physical environment. Passthrough techniques are intended to address this limitation by leveraging outward-facing cameras to reconstruct the images that would otherwise be seen by the user without the headset. This is inherently a real-time view synthesis challenge, since passthrough cameras cannot be physically co-located with the user’s eyes. Existing passthrough techniques suffer from distracting reconstruction artifacts, largely due to the lack of accurate depth information (especially for near-field and disoccluded objects), and also exhibit limited image quality (e.g., being low resolution and monochromatic). In this paper, we propose

the first *learned* passthrough method and assess its performance using a custom VR headset that contains a stereo pair of RGB cameras. Through both simulations and experiments, we demonstrate that our learned passthrough method delivers superior image quality compared to state-of-the-art methods, while meeting strict VR requirements for real-time, perspective-correct stereoscopic view synthesis over a wide field of view for desktop-connected headsets.

CCS CONCEPTS

• **Computing methodologies** → **Mixed / augmented reality; Machine learning; Image-based rendering.**

KEYWORDS

Passthrough, Real-Time View Synthesis, Virtual Reality

ACM Reference Format:

Lei Xiao, Salah Nouri, Joel Hegland, Alberto Garcia Garcia, and Douglas Lanman. 2022. NeuralPassthrough: Learned Real-Time View Synthesis for VR. In *Special Interest Group on Computer Graphics and Interactive Techniques Conference Proceedings (SIGGRAPH ’22 Conference Proceedings)*, August 7–11, 2022, Vancouver, BC, Canada. ACM, New York, NY, USA, 9 pages. <https://doi.org/10.1145/3528233.3530701>

Permission to make digital or hard copies of part or all of this work for personal or classroom use is granted without fee provided that copies are not made or distributed for profit or commercial advantage and that copies bear this notice and the full citation on the first page. Copyrights for third-party components of this work must be honored. For all other uses, contact the owner/author(s).
SIGGRAPH ’22 Conference Proceedings, August 7–11, 2022, Vancouver, BC, Canada
© 2022 Copyright held by the owner/author(s).
ACM ISBN 978-1-4503-9337-9/22/08.
<https://doi.org/10.1145/3528233.3530701>

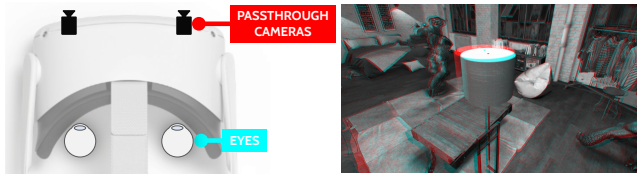


Figure 2: *Left:* Typically, VR passthrough cameras are located several centimeters away from the user’s eyes. *Right:* Separation between the cameras and the eyes requires significant viewpoint changes to be resolved by the passthrough algorithm. Here the right-eye camera image (shown in red) is compared to what should be seen by the user’s right eye (shown in cyan).

1 INTRODUCTION

Virtual reality (VR) head-mounted displays (HMDs) provide nearly complete visual immersion, using a pair of near-eye displays to create wide-field-of-view, stereoscopic images. However, such immersion comes at the cost of visual isolation from the user’s physical environment. For certain applications, a direct view of the nearby surroundings is necessary. To this end, augmented reality (AR) uses near-eye displays to support *optical see-through*. Yet, modern AR displays achieve limited fields of view, unlike blocked-light VR; thus, *video see-through* VR has been proposed as a solution, using *passthrough* algorithms to transform imagery collected by outward-facing cameras to enable the user to see their surroundings.

In practice, VR passthrough systems do not directly pass through anything. Rather, they must accomplish the difficult task of reprojecting camera images to appear from the user’s perspective. This is often approximated, with Krajancich et al. [2020] showing the value of updating reconstructions to track the user’s moving pupils. While pupil-tracked passthrough may be the ultimate goal, state-of-the-art techniques, such as *Passthrough+* [Chaurasia et al. 2020], reproject camera data to the nominal position of the eyes, while accepting any artifacts resulting from the computational limits.

Real-time view synthesis lies at the core of achieving compelling passthrough experiences. While this is a challenging problem itself [Mildenhall et al. 2019, 2020; Zhou et al. 2018], VR headsets present particularly daunting requirements that cannot be supported by many modern methods. Namely, commercial VR displays are stereoscopic, refresh at 72-144 frames per second, and support wide fields of view ($>90^\circ$, horizontally). For VR passthrough, a typical scenario involves a user’s manipulating near-field objects with their own hands and observing dynamic environments, resulting in large regions with missing data, due to disocclusions, and preventing offline reconstruction from prior observations.

Given these algorithmic challenges, headset designers can assist passthrough by placing cameras as close to the user’s eyes as possible, asking the algorithm to make only modest changes. Yet, as shown in Figure 2, cameras cannot be co-located with the user’s eyes. Thus, in this paper, we optimize the performance of a minimal passthrough architecture: placing a stereo pair of RGB cameras on the front of a VR headset (see Figure 1). Consistent with Chaurasia et al. [2020], we identify that such a configuration offers a practical trade-off between hardware and algorithmic complexity. However,

unlike prior works, we consider the optimal placement of the cameras to work in concert with the passthrough algorithm, exploring how the baseline can be adjusted to mitigate reprojection artifacts.

We aim to find an efficient, high-quality method for real-time stereoscopic view synthesis from stereo inputs. Being the closest prior work, we seek to address the limitations of Chaurasia et al. [2020], which applies a traditional 3D computer vision pipeline: for each frame, a sparse point cloud is reconstructed and processed to produce meshes for reprojection. In contrast, we introduce *NeuralPassthrough* to leverage recent advances in deep learning, solving passthrough as an image-based neural rendering problem. Specifically, we jointly apply learned stereo depth estimation and image reconstruction networks to produce the eye-viewpoint images via an end-to-end approach, one that is tailored for today’s desktop-connected VR headsets and their strict real-time requirements. The source code and pretrained models will be available at <https://research.facebook.com/publications/neural-passthrough/>, pending institutional approval. Our primary technical contributions include the following:

- We build a VR headset with an adjustable stereo camera baseline, optimized for evaluating view synthesis methods.
- We analyze the impact of camera placement on VR passthrough image quality; our analysis reveals that key disocclusions can be mitigated by adopting wider camera baselines than the user’s interpupillary distance (IPD) — a design optimization that diverges from current consumer products.
- We demonstrate the first learned view synthesis method tailored for real-time VR passthrough, suppressing key artifacts and achieving higher image quality than prior methods.

2 RELATED WORK

2.1 Classical Methods for View Synthesis

Early work on light field imaging addresses view synthesis as an interpolation problem, resampling captured rays to generate novel views [Gortler et al. 1996; Levoy and Hanrahan 1996]. However, by requiring a dense set of input views, such methods are not well suited for VR passthrough. View synthesis from sparse views gained much attention in graphics rendering [Chen and Williams 1993; Oculus 2016], computational photography [Hedman et al. 2017; Shade et al. 1998; Zitnick et al. 2004] and displays [Chapiro et al. 2014; Didyk et al. 2013]. Most of these methods require rendered depth as input, allow limited viewpoint changes, or run offline.

To our knowledge, *Passthrough+* [Chaurasia et al. 2020] is the only prior work that directly addresses VR passthrough. It is specifically tailored for mobile VR applications, but achieves limited image quality. In contrast, our method focuses on desktop-connected VR headsets, leveraging more compute resources while continuing to be strictly constrained by the same real-time requirements.

2.2 Learning-based Methods for View Synthesis

Significant recent progress has been made in learning-based view synthesis, which can be grouped according to the inputs: single views [Kopf et al. 2020; Shih et al. 2020; Wiles et al. 2020]; stereo views [Zhou et al. 2018]; multiple views [Flynn et al. 2019; Kalantari et al. 2016; Mildenhall et al. 2019, 2020]; multiview videos [Broxton et al. 2020]; and RGB-D captures [Aliev et al. 2020; Martin-Brualla

et al. 2018]. In closely related work, Zhou et al. [2018] represent a static scene with multiplane images (MPIs) generated from stereo pairs. Once generated, MPIs can be reused to efficiently render a range of output views. DeepView [Flynn et al. 2019] generates MPIs from multiview images using learned gradient descent. While MPIs allow for efficient rendering of dynamically varying viewpoints, generating an MPI from input images can be computationally expensive. Furthermore, MPIs can only render a limited range of views, i.e., perceptible artifacts often appear when the output view is relatively far from the reference views. Mildenhall et al. [2019] mitigate this problem by building multiple MPIs from a broad set of input views, which are blended together to create the output view, albeit with significant computational overhead (due to multiple MPI generation/rendering steps and costly 3D convolutional networks). Martin-Brualla et al. [2018] does real-time neural view synthesis, but it requires textured 3D reconstruction from a performance capture system as input and is limited to human scenes. Aliev et al. [2020] introduces neural point-based representation but it requires a raw point cloud as input and presents limited quality.

A prominent line of recent research relates to neural radiance fields (NeRFs) [Mildenhall et al. 2020]. NeRFs represent a scene as an implicit function encoded by multilayer perceptrons (MLPs). NeRF-inspired approaches have led to rapid advances in view synthesis; however, none of these recent works directly address the unique challenges of VR passthrough. Specifically, many NeRF-derived methods rely on a dense set of views. More significantly, these methods incur prohibitive computational costs for per-scene optimization and volume rendering. Despite recent work to decrease these costs [Garbin et al. 2021; Hedman et al. 2021; Liu et al. 2020; Reiser et al. 2021; Yu et al. 2021a], NeRF-based methods still do not appear practical for VR passthrough. Similarly, other works have attempted to reduce the number and range of input views [Jain et al. 2021; Yu et al. 2021b; Zhang et al. 2020], to support dynamic scenes [Gao et al. 2021; Pumarola et al. 2021] and to be generalizable [Guo et al. 2022; Yu et al. 2021b]; however, these lines of research have also fallen short on the crucial real-time requirement.

3 NEURAL PASSTHROUGH

In this section, we describe our neural passthrough system, including both optimizing the configuration of our hardware prototype (Section 3.1) and the aspects of designing and training our real-time neural view synthesis method (Sections 3.2 and 3.3, respectively).

3.1 Optimizing the Hardware Configuration

As outlined in Section 1, we focus on constructing a passthrough capture system with minimal hardware (i.e., using a pair of stereo RGB cameras as the only input). As such, the hardware design challenge can be posed as an optimization problem: where should the cameras be placed to best support view synthesis algorithms?

We define the objective as *maximizing the information captured from the 3D scene, by the stereo cameras, that is necessary for reconstructing the target novel views*. In other words, we want to select the stereo camera placement to minimize the extent of the *disocclusion* regions (i.e., the set of 3D points that would be visible in the target novel views but that are occluded in the input views and, thus, cannot be faithfully recovered by view synthesis).

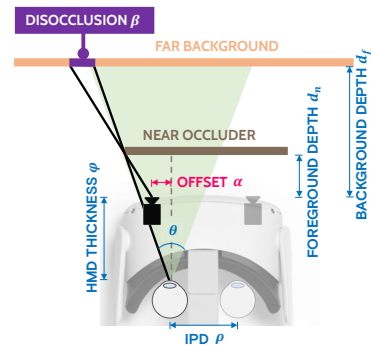


Figure 3: The extent of disocclusion regions (i.e., scene points that should be seen by the user’s eyes but are occluded from the camera’s perspective) depends on the VR headset construction, the position of the user’s eyes, and the physical scene geometry. In this simplified model, the width β of the disocclusion region is determined for a scene containing a near-field occluder and a far background plane. See Section 3.1 for an application of this model to the optimization of stereo camera baselines for VR passthrough.

In Figure 3, we analyze the parameters that affect disocclusion. Note that, since we only consider a pair of cameras on the front surface of a HMD, we constrain both cameras to be vertically located on the same plane as the nominal eye positions and the optical centers of the viewing optics. Both cameras face directly forward and are further constrained to be symmetric about the HMD center. Under these constraints, the free parameters defining the camera placement reduce to just the horizontal offset α between each camera and its corresponding eye. Intuitively, one might consider setting α to zero, minimizing the distance between the input and target viewpoints. However, we propose to *increase* α (to a certain extent) to reduce the degree of disocclusions and, thus, provide some assistance to the view synthesis algorithm.

Applying the model in Figure 3, disocclusion appears in the target view due to the viewpoint difference between the camera and the eye. The width of the disocclusion region β is given by

$$\beta = \max\left(0, \varphi \tan\left(\frac{\theta}{2}\right) - \alpha\right) \cdot \left(\frac{d_f}{d_n} - 1\right) \quad (1)$$

where φ denotes the distance between the camera and the eye along the depth axis (i.e., the HMD thickness), d_n and d_f denote the depth of the near occluder and the background respectively ($d_n < d_f$), and $\theta \in [0, \pi)$ measures the angular region within which the disocclusion is aimed to be eliminated. Note that, under our stereo camera constraints, only horizontal disocclusion can be reduced. From Eq. (1), clearly, when $\alpha \geq \varphi \tan\frac{\theta}{2}$, disocclusion β will disappear. Given ρ is the target interpupillary distance (IPD), the required minimal stereo camera baseline becomes $\rho + 2\varphi \tan\frac{\theta}{2}$.

From Eq. (1), we also note that reducing HMD thickness φ could reduce disocclusion β . This suggests that the passthrough problem can benefit from more compact headset designs, such as those introduced by Maimone and Wang [2020]. In addition, disocclusion β increases when foreground objects are closer.

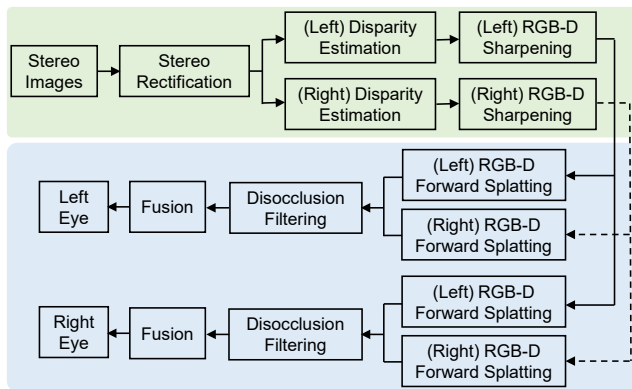


Figure 4: Overview of the *NeuralPassthrough* algorithm.

While this simplified model motivates slightly increasing the camera baseline in comparison to the user’s IPD, this design choice does potentially introduce other issues. Following Figure 3, as the left-hand camera moves to the left, it may reduce or even eliminate disocclusion on the left side of the occluder. However, disocclusion may be introduced on the right side. We observe that, since we have a stereo camera pair, increasing disocclusion in this manner may be somewhat compensated by utilizing observations from the other camera. Many anticipated near-field objects in VR use cases, such as hands and handheld implements, are compact enough such that the other camera can contribute to observing what would otherwise become a hidden surface. Thus, we have elected to increase our camera baseline in our prototype HMD in this manner. Experimental results are given in the supplementary material.

As shown in Figure 1, our prototype includes stereo RGB cameras (from Azure Kinect DK [2021]) attached to an Oculus Rift S headset [2021]. The camera enclosures are removed and some electrical components are folded away from the front of the headset. We place the stereo cameras on a linear translation stage, allowing the baseline to be adjusted. The supported baseline ranges from 5.4cm to 10cm. For the results shown in this paper, we selected a 10cm baseline. That supports an angular region $\theta = 25^\circ$, where the disocclusion is eliminated for an IPD of $\rho = 6$ cm, or, equivalently, $\theta = 18^\circ$ for an IPD of $\rho = 7$ cm. The distance between the cameras and the eyes (along the depth axis) is $\varphi = 9.3$ cm. Each RGB camera runs at 30Hz with a resolution of 1280×720 and a 90° field of view.

3.2 Learned, Real-Time View Synthesis

In this section, we define the *NeuralPassthrough* algorithm. This method addresses passthrough as an image-based rendering problem, solved separately per frame, taking stereo camera images as input and producing stereo images for the target eye views.

A block diagram of the method is provided in Figure 4. At a high level, the method represents the scene with 2D color and depth (RGB-D) images. A depth map is estimated at *each* of the input views by deep-learning-based disparity estimation (Section 3.2.1). The RGB-D pixels of both input views are then splatted to each target view (Section 3.2.3) before being fed into a neural network for final view reconstruction (Section 3.2.5). To reduce splatting artifacts due to the ambiguity of depth at discontinuities (e.g., “flying” pixels),

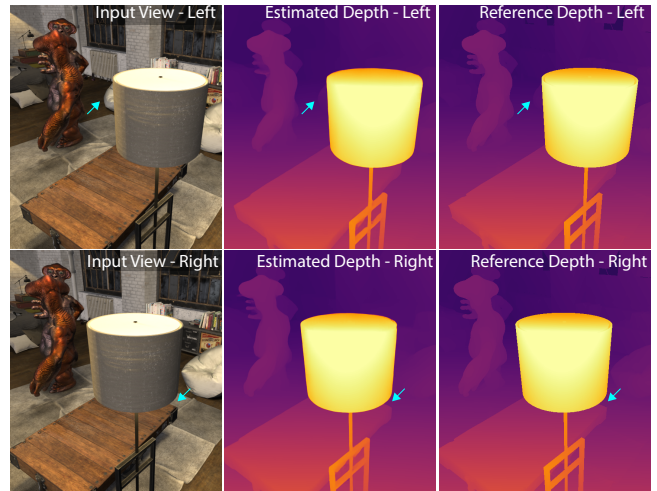


Figure 5: Depth estimation example. Note that the depths, estimated by the algorithm in Section 3.2.1, well approximate the reference depths. The arrows indicate regions that are only visible in one of the stereo inputs, but where plausible depth is estimated from monocular depth cues.

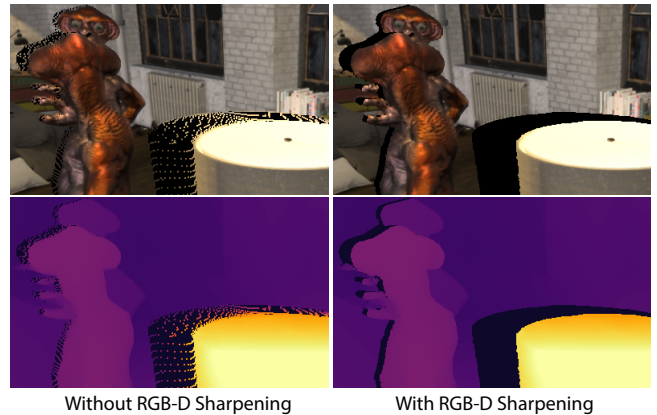


Figure 6: Applying the RGB-D sharpening operation, following Section 3.2.2, suppresses “flying-pixel” artifacts and produces cleaner depth maps. As shown on the left-hand side, without RGB-D sharpening, “flying pixels” are produced within the disocclusion regions (i.e., the background RGB areas surrounding the edge of the lamp shade and the boundaries of the characters).

the method filters the RGB-D data at each input view (Section 3.2.2) before the splatting operation. The method further applies processing to reduce disocclusion artifacts in the splatted RGB values (Section 3.2.4) before passing them to the final reconstruction.

3.2.1 Depth Estimation. We first rectify the input color image pairs, reducing disparity estimation from a 2D correspondence-matching problem to a more efficient 1D matching problem. In contrast to *Passthrough+* [Chaurasia et al. 2020], which estimates scene depth from motion vectors produced by video encoding hardware, we

leverage neural approaches to produce higher quality depth maps. Specifically, we apply the *RAFT-Stereo* algorithm [Lipson et al. 2021] to estimate a disparity map at each of stereo input views, which are then converted to inverse depth maps using pre-calibrated camera parameters. We denote the rectified input color and the estimated inverse depth as $\{c_l, c_r\}$ and $\{d_l, d_r\}$ respectively, where the subscript l and r indicate left and right views respectively.

Figure 5 shows an example of the estimated depth maps recovered from stereo inputs, which accurately approximate the reference depth maps. Importantly, for regions that are only visible in one of the input views, the depth estimation network can still produce reasonable results from neighboring pixels and from monocular depth cues learned during training — differing from the motion-vector-based depth in *Passthrough+* [Chaurasia et al. 2020] and the plane-sweep-volume approach in MPI-based methods [Zhou et al. 2018]. This is one of the key reasons that we choose to estimate the depth at *each* input view, since the two depth maps provide complementary information of the scene geometry.

3.2.2 RGB-D Sharpening. While the estimated depth maps visually align with the corresponding color images, if they were directly used for view reprojection (Section 3.2.3), “flying pixels” would occur at the disoccluded regions in the reprojected images, due to depth ambiguity at depth discontinuities (see Figure 6). To reduce this problem, we propose sharpening the color images and estimated depth maps along depth discontinuities. Specifically, we detect the depth edges with Sobel filter followed by morphological dilation, and then set the RGB-D values of the edge pixels to that of their nearest-neighbor, non-edge pixels. We emphasize that another benefit of such RGB-D sharpening is that it helps produce clean depths in the splatted image space, which are important for the following disocclusion filtering step to work properly (Section 3.2.4).

3.2.3 Forward Splating. We elect to apply a neural network to reconstruct the color image, at each target eye viewpoint, from the color and recovered depth for the input stereo views. To reduce the required receptive field of the neural network, we first warp each input view to the target view. Since the depths are estimated for the input views, forward warping is required. Compared to backward warping, forward warping is more prone to introducing holes due to disocclusion; similarly, with forward warping, multiple source pixels can map to the same pixel in the warped image space, due to newly introduced occlusions. Both failure cases often occur for VR passthrough applications. In this section, we focus on the issue caused by newly introduced occlusions, leaving the discussion regarding disocclusion holes until Section 3.2.4.

Fortunately, we have the estimated depth at each input view, providing visibility information for each 3D point. We employ the *softmax* splating method that was originally developed for video frame interpolation [Niklaus and Liu 2020]. This method blends the pixels that were mapped to the same target pixel, applying pixel-wise importance weights defined as a measure of occlusion. In our implementation, we define the importance weights w to be a function of the estimated inverse depth d , given by

$$w = 36 \left(\frac{d - d_{min}}{d_{max} - d_{min}} + \frac{1}{9} \right) \quad (2)$$

ALGORITHM 1: Full Disocclusion Filtering

Input: Color image \bar{c} , inverse depth \bar{d} , occlusion mask \bar{m} , kernel k
Output: Filtered color image c^*

```

for each pixel  $i$  do
  if  $\bar{m}(i)$  is 0 then
     $c^*(i) = \bar{c}(i)$ 
  else
     $\bar{d}_{min}^N, \bar{d}_{max}^N, c_{acc}, w_{acc} = \text{MAX}, \text{MIN}, 0, 0$ 
    for each pixel  $j$  in local neighborhood  $\mathcal{N}_i$  do
      if  $\bar{d}(j) > 0.01$  then
         $\bar{d}_{min}^N, \bar{d}_{max}^N = \min(\bar{d}_{min}^N, \bar{d}(j)), \max(\bar{d}_{max}^N, \bar{d}(j))$ 
    for each pixel  $j$  in local neighborhood  $\mathcal{N}_i$  do
      if  $\bar{d}(j) > 0.01$  and  $\bar{d}(j) < 0.5(\bar{d}_{min}^N + \bar{d}_{max}^N)$  then
         $c_{acc} += \bar{c}(j) \cdot k(i, j)$ 
         $w_{acc} += k(i, j)$ 
    if  $w_{acc} > 0$  then
       $c^*(i) = c_{acc} / w_{acc}$ 
    else
       $c^*(i) = \bar{c}(i)$ 

```

where d_{min} and d_{max} are the minimum and maximum of the inverse depth map d , and the heuristic constants are chosen to map the weights to the range [4, 40], which works well in our experiments. The metric w assigns higher weights to the source pixels closer to the cameras (in the warped image space). We denote the splatted color and inverse depth as $\{\bar{c}_l, \bar{c}_r\}$ and $\{\bar{d}_l, \bar{d}_r\}$, respectively.

3.2.4 Disocclusion Filtering. The forward-splatted images at the target views typically contain holes due to disocclusions, as shown in Figure 7. In this section, we describe our approach to address this issue. We divide the disocclusion holes into two categories and treat them separately: *partial disocclusion*, defined as the holes that occur in only one of the splatted images (i.e., either \bar{c}_l or \bar{c}_r), and *full disocclusion*, defined as the holes that occur in both \bar{c}_l and \bar{c}_r .

Partial disocclusion can be removed by blending \bar{c}_l and \bar{c}_r :

$$\begin{aligned} \hat{c}_l &= (1 - m_l) \odot \bar{c}_l + m_l \odot \bar{c}_r \\ \hat{c}_r &= (1 - m_r) \odot \bar{c}_r + m_r \odot \bar{c}_l \end{aligned} \quad (3)$$

where \odot denotes the Hadamard product, and the pixel-wise masks m_l and m_r are defined on the splatted inverse depth \bar{d}_l and \bar{d}_r , as

$$m_l = \begin{cases} 1 & \text{if } \bar{d}_l < \epsilon \\ 0 & \text{otherwise} \end{cases}, \quad m_r = \begin{cases} 1 & \text{if } \bar{d}_r < \epsilon \\ 0 & \text{otherwise} \end{cases} \quad (4)$$

where $\epsilon = 0.1$ and $\{m_l, m_r\}$ indicate the zero-valued pixels in the splatted inverse depth maps $\{\bar{d}_l, \bar{d}_r\}$. Partial disocclusion removal results are shown in Figure 7.

Full disocclusions can not be faithfully recovered as the input stereo inputs contain no information for those regions. As reviewed in Section 2.2, prior work in 3D photography [Shih et al. 2020] resolves disocclusions via context-aware image inpainting. We find that for *static* images visually acceptable results can be hallucinated; but, if applied to our *dynamic* passthrough problem, this approach will introduce temporal flickering into the output videos. Furthermore, advanced image inpainting techniques [Liu et al. 2018; Shih et al. 2020] are typically computationally expensive, hindering their utility for our real-time application.

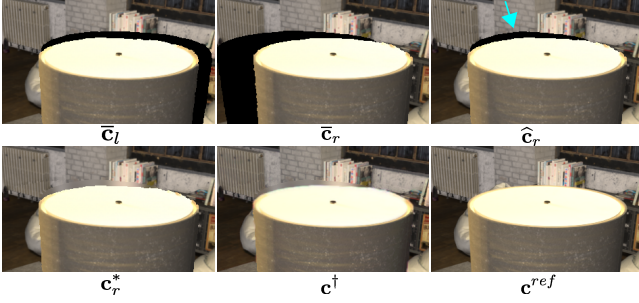


Figure 7: Example results for disocclusion filtering, as defined in Section 3.2.4. \bar{c}_l and \bar{c}_r are the forward-splatted color images, as taken from the input left and right view, respectively (see Section 3.2.3). \hat{c}_r and c_r^* are the right view after partial (Eq. (3)) and full disocclusion filtering (Eq. (5)), respectively. c^\dagger is the final reconstruction (Eq. 6), and c^{ref} is the reference for the target view. The arrows point to regions with full disocclusion holes.

As an alternative, we propose depth-assisted, anisotropic low-pass filtering to produce stable results efficiently. We observe that the disoccluded regions are more often missing information from background objects rather than from foreground occluders; as a result, our method fills in the disoccluded pixels using only the smoothed colors of *relatively far* objects within the local neighborhood. The method details are given by in Eq. (5) and Algorithm 1:

$$\begin{aligned} \hat{\mathbf{m}} &= \mathbf{m}_l \odot \mathbf{m}_r \\ c_l^* &= \text{full_disocclusion_filtering}(\bar{c}_l, \bar{\mathbf{d}}_l, \hat{\mathbf{m}}, \mathbf{k}) \\ c_r^* &= \text{full_disocclusion_filtering}(\bar{c}_r, \bar{\mathbf{d}}_r, \hat{\mathbf{m}}, \mathbf{k}) \end{aligned} \quad (5)$$

The mask $\hat{\mathbf{m}}$ indicates whether a pixel is fully disoccluded. \mathbf{k} denotes a low-pass kernel (which in our implementation is a zero-mean 2D Gaussian filter with size 29×29 and a standard deviation of 7 pixels). For experimental evaluation of the benefits of the filtering operations, see Table 2.

3.2.5 Fusion. Our pipeline concludes by feeding the disocclusion-filtered images to a neural network for final reconstruction at the target eye views, as given by

$$c^\dagger = \text{fusion}(c_l^*, c_r^*) \quad (6)$$

where the fusion network is a lightweight U-Net with skip connections, comprising the specific architecture in Table 1. Note that the fusion network runs once for each of the two target eye views, as illustrated in Figure 4. We find that fusion is necessary to further reduce reprojection errors and aliasing artifacts in c_l^* and c_r^* .

3.3 Training

The training loss function for *NeuralPassthrough* is defined as

$$10 \| (1 - \hat{\mathbf{m}}) \odot (c^\dagger - c^{ref}) \|_1 - \| (1 - \hat{\mathbf{m}}) \odot \text{ssim}(c^\dagger, c^{ref}) \|_1 \quad (7)$$

where *ssim* is the structural similarity index measure [Wang et al. 2004]. We apply the mask $(1 - \hat{\mathbf{m}})$ to exclude the full disocclusion regions from the loss, preventing inpainting at those regions (which may lead to inconsistent temporal and left/right completions that,

Table 1: Each layer of the fusion network (Section 3.2.5) is a 2D convolution followed by relu activation. The operators concat, down, and up, represent concatenation, average pooling, and bilinear upsampling, respectively.

Layer	Input Tensor	Channels In/Out
conv0	concat(c_l^* , c_r^*)	6/16
conv1	conv0	16/16
conv2	down(conv1)	16/32
conv3	conv2	32/32
conv4	down(conv3)	32/64
conv5	conv4	64/64
conv6	concat(up(conv5), conv))	96/32
conv7	layer6	32/32
conv8	concat(up(conv7), conv1)	48/16
conv9	conv8	16/16
conv10	conv9	16/3

Table 2: Quality comparisons for *NeuralPassthrough* (Ours) on synthetic datasets. Average PSNR (dB), SSIM and ST-RRED are reported. Higher PSNR and SSIM, and lower ST-RRED indicate better quality.

	PSNR \uparrow	SSIM \uparrow	ST-RRED \downarrow
MPI [Zhou et al. 2018]	27.38	0.8818	105.74
Ours	30.74	0.9579	51.78
Ours (trained without Eq. 5)	28.66	0.9475	95.33
Ours (trained without Eq. 3, 5)	29.02	0.9456	99.33

in turn, could degrade the user experience, especially due to the limited capacity (by design) of the fusion network in Section 3.2.5). The stereo depth network reapplies the pre-trained *RAFT-Stereo* model with frozen weights during training.

We train the method on a synthetic dataset with 80 random scenes, similar to the ones in Xiao et al. [2018]. Each scene includes 3D scans of sculptures from the Louvre as well as spheres and cubes, that are randomly textured and placed in 3D space with varying depths. The unnatural geometry and appearance makes the training data substantially different from the synthetic and real scenes we test in the paper. Example scenes are provided in the supplementary material. For each scene, we render 20 image sequences with a resolution of 512×512 and rendered at varying viewpoints (i.e., two views serve as the input stereo pair, with a 10cm baseline, and the rest are the target output views that are 9.3cm behind the input views and with baselines ranging from 4.8cm to 8.0cm). Note that the trained network can be applied to other camera and IPD configurations, as well as to different input resolutions, at test time. We train the method in Pytorch using the ADAM optimizer with default parameters for 120 epoches.

4 RESULTS

4.1 Real-Time Implementation

After training, we implement our full, optimized inference method in C++ using CUDA/CuDNN, integrating it with the Oculus Rift SDK for real-time passthrough demonstrations. We test the method

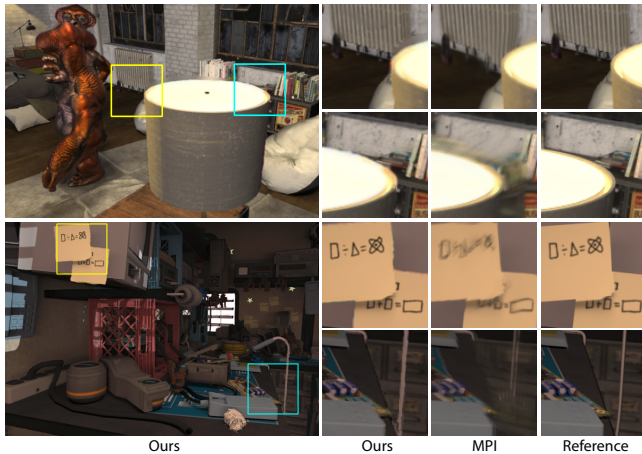


Figure 8: Comparisons on synthetic data. For the *DanceStudio* scene (top), our PSNR and SSIM are 34.28dB and 0.97, while MPI [Zhou et al. 2018] achieves 29.69dB and 0.90. For the *ElectronicRoom* scene (bottom), ours are 30.06dB and 0.95, while MPI achieves 24.42dB and 0.86. The MPI results present obvious artifacts (e.g., stretching and repeated textures at disocclusions).

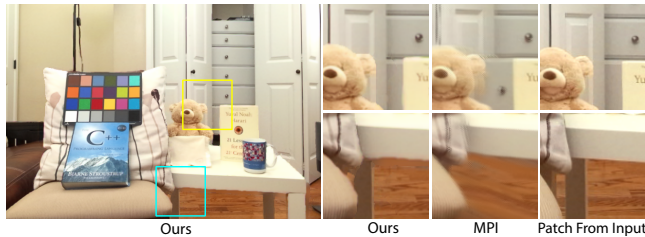


Figure 9: Qualitative comparisons on data captured by our prototype headset. Our method does not produce texture stretching artifacts, while MPI [Zhou et al. 2018] tends to, while also failing to reconstruct the table leg.

on a desktop with an Intel Xeon W-2155 CPU and dual Nvidia Titan V GPUs. Each GPU is responsible for one depth estimation and one eye-view reconstruction. The method runs at 32ms per frame at a resolution of 1280×720 for the two eye views, with depth estimation at 24.0ms, RGB-D sharpening at 0.3ms, forward-splatting at 0.8ms, disocclusion filtering at 0.9ms, and the fusion network at 5.6ms.

While we report these run times for our per-frame processing pipeline, we see opportunities for further improvement. For example, we could run the depth estimation at a lower frame rate (e.g., 30Hz), but run the color reconstruction operations (i.e., forward splatting, disocclusion filtering, and fusion, which take 7.3ms in total) at a higher frame rate (e.g., 72Hz or the native refresh rate of the displays). In this manner, the more efficient color reconstruction pipeline could account for the current estimate of the head pose, while reusing the latest depth estimates. Notably, such a *decoupled* framework is similar to *Passthrough+*, which reconstructs the textured meshes at 30Hz, but renders the eye buffers at 72Hz.

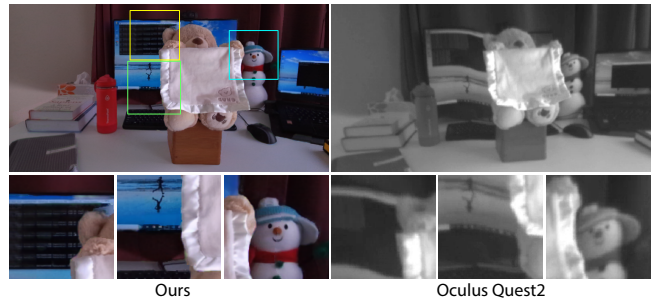


Figure 10: Visual comparisons between our method and Oculus Quest 2, which is closely related to *Passthrough+* [Chaurasia et al. 2020].

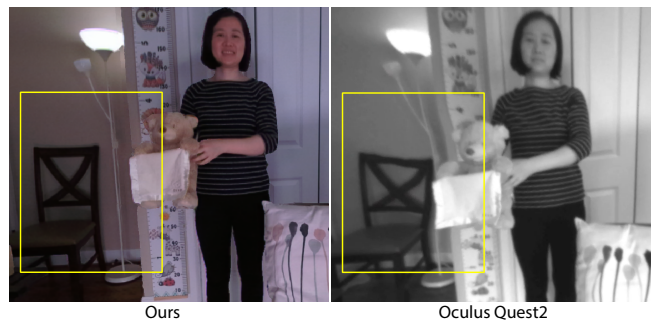


Figure 11: Visual comparisons between our method and Oculus Quest 2 on a dynamic scene. Our method does not show severe distortions, whereas Quest 2 does as highlighted.

4.2 Quality Comparisons

As there is little recent work on real-time view synthesis, we compare to the representative MPI method [Zhou et al. 2018], which also takes stereo images as inputs. MPI requires several seconds to generate the multiplane representation and another several seconds to render stereo eye views (at a resolution of 1280×720 using TensorFlow with our system). Although follow-up MPI works exist with improved quality [Mildenhall et al. 2019; Srinivasan et al. 2019], these approaches are substantially slower due to the need to generate/render multiple MPIs per frame and the use of 3D convolutional networks, making them even less applicable to VR passthrough.

For image quality comparisons, we render two datasets for 3D environments with dynamic objects (*DanceStudio* and *ElectronicRoom*). Each dataset contains 5 videos with simulated VR head movements, each containing 30 frames at a resolution of 1280×720 . For each frame, we render input stereo views (with a 10cm baseline) and target eye views (with a 6cm IPD and depth-axis offset of 9.3cm). These scenes differ in appearance from our static training datasets.

We evaluate the methods using PSNR, SSIM [Wang et al. 2004] and Spatio-Temporal Entropic Difference (ST-RRED) [Soundararajan and Bovik 2012], where the latter is for video quality and temporal stability assessment. As reported in Table 2, our method outperforms MPI by a large margin on all metrics. Example result are shown in Figure 8. Notably, MPI presents more obvious

artifacts, especially distortion, stretching, and repeated textures at disocclusion regions.

We qualitatively compare these methods using real data captured by our prototype, as shown in Figure 9. Since we can not capture the ground truth reference images at the target eye views, we provide the closest patches from the input views as a visual reference.

As reviewed in Sections 1, the closest related work to our *NeuralPassthrough* is *Passthrough+* [Chaurasia et al. 2020], which is the predecessor to the current commercial solution applied in Oculus Quest 2. As this commercial implementation is unavailable, and its camera images are not accessible via the Oculus SDK, we capture scenes with similar camera trajectories using our prototype and the Quest 2, allowing for qualitative visual comparisons. Example results are shown in Figures 10 and 11. We observe that the main limitation of Oculus Quest 2 is that the reconstructed mesh can be inaccurate at depth discontinuities and within disocclusion regions, causing noticeable distortion and stretching artifacts. In contrast, our method produces more accurate results, while also allowing for color outputs with higher resolution. Please refer to the supplementary material for video results and comparisons.

5 LIMITATIONS AND FUTURE WORK

The quality of our results is partly affected by the quality of our real-time depth estimation. While the depth estimation module produces reasonable results in most circumstances, it may fail for objects with challenging geometric details, for view-dependent materials, or when the monocular depth cues are lacking. Our results may also present blending artifacts when the input stereo views contain mismatched colors due to severe view-dependent reflections, especially when they appear together with disocclusion. Examples of these failure cases are shown in Figure 12.

Future improvements in real-time depth estimation may benefit our approach, updating the associated step of our pipeline. In future work, active depth sensors may provide instant depth generation and improve depth estimation for regions where stereo recovery does not work well (e.g. regions with little texture, difficult partial disocclusions, or view-dependent effects). To enable this work, our hardware prototype already incorporates depth sensors.

Oculus Quest 2 passthrough results suffer from severe distortion artifacts, however they typically appear temporally stable, partly due to their low resolution, but also due to their multi-frame reconstruction method. As future work, we anticipate leveraging multiple frames to further improve spatial quality and temporal consistency.

6 CONCLUSION

This paper takes a first step towards bringing the latest developments in neural view synthesis to the specific domain of VR passthrough. With VR recently seeing wider adoption, we believe improved passthrough technologies are necessary to unlock a broad set of mixed reality applications — seamlessly blending virtual objects with the user’s physical surroundings. Throughout this paper we have emphasized that, while neural view synthesis is an increasingly well studied topic, VR applications set a much higher bar on performance. To deliver compelling VR passthrough, the field will need to make significant strides both in image quality (i.e., suppressing notable warping and disocclusion artifacts), while meeting the

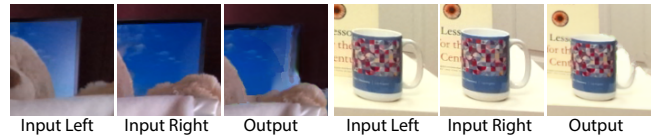


Figure 12: Example failure cases on real data. Our system may produce artifacts for objects with significant view-dependent reflections (monitor corner) or with complex geometry and ambiguities in stereo matching (mug handle).

strict real-time, stereoscopic, and wide-field-of-view requirements. Tacking on the further constraint of mobile processors for wearable computing devices means that there truly is a long road ahead.

REFERENCES

2021. Azure Kinect DK. <https://azure.microsoft.com/en-us/services/kinect-dk/>
2021. Rift-S VR. <https://www.oculus.com/rift-s/features/>
- Kara-Ali Aliev, Artem Sevastopolsky, Maria Kolos, Dmitry Ulyanov, and Victor Lempitsky. 2020. Neural point-based graphics. In *European Conference on Computer Vision*. Springer, 696–712.
- Michael Broxton, John Flynn, Ryan Overbeck, Daniel Erickson, Peter Hedman, Matthew Duvall, Jason Dourgarian, Jay Busch, Matt Whalen, and Paul Debevec. 2020. Immersive light field video with a layered mesh representation. *ACM Transactions on Graphics (TOG)* 39, 4 (2020), 86–1.
- Alexandre Chapiro, Simon Heinzele, Tuğ Ozan Aydın, Steven Poulakos, Matthias Zwicker, Aljosa Smolic, and Markus Gross. 2014. Optimizing stereo-to-multiview conversion for autostereoscopic displays. In *Computer graphics forum*, Vol. 33. Wiley Online Library, 63–72.
- Gaurav Chaurasia, Arthur Nieuwoudt, Alexandru-Eugen Ichim, Richard Szeliski, and Alexander Sorkine-Hornung. 2020. Passthrough+ Real-time Stereoscopic View Synthesis for Mobile Mixed Reality. *Proceedings of the ACM on Computer Graphics and Interactive Techniques* 3, 1 (2020), 1–17.
- Shenchang Eric Chen and Lance Williams. 1993. View interpolation for image synthesis. In *Proceedings of the 20th annual conference on Computer graphics and interactive techniques*. 279–288.
- Piotr Didyk, Pitchaya Sitthi-Amorn, William Freeman, Frédo Durand, and Wojciech Matusik. 2013. Joint view expansion and filtering for autostereoscopic 3D displays. *ACM Transactions on Graphics (TOG)* 32, 6 (2013), 1–8.
- John Flynn, Michael Broxton, Paul Debevec, Matthew DuVall, Graham Fyffe, Ryan Overbeck, Noah Snavely, and Richard Tucker. 2019. Deepview: View synthesis with learned gradient descent. In *Proceedings of the IEEE/CVF Conference on Computer Vision and Pattern Recognition*. 2367–2376.
- Chen Gao, Ayush Saraf, Johannes Kopf, and Jia-Bin Huang. 2021. Dynamic View Synthesis from Dynamic Monocular Video. *arXiv preprint arXiv:2105.06468* (2021).
- Stephan J Garbin, Marek Kowalski, Matthew Johnson, Jamie Shotton, and Julien Valentin. 2021. Fastnerf: High-fidelity neural rendering at 200fps. In *Proceedings of the IEEE/CVF International Conference on Computer Vision*. 14346–14355.
- Steven J Gortler, Radek Grzeszczuk, Richard Szeliski, and Michael F Cohen. 1996. The lumigraph. In *Proceedings of the 23rd annual conference on Computer graphics and interactive techniques*. 43–54.
- Pengsheng Guo, Miguel Angel Bautista, Alex Colburn, Liang Yang, Daniel Ulbricht, Joshua M Susskind, and Qi Shan. 2022. Fast and Explicit Neural View Synthesis. In *Proceedings of the IEEE/CVF Winter Conference on Applications of Computer Vision*. 3791–3800.
- Peter Hedman, Suhil Alsison, Richard Szeliski, and Johannes Kopf. 2017. Casual 3D photography. *ACM Transactions on Graphics (TOG)* 36, 6 (2017), 1–15.
- Peter Hedman, Pratul P Srinivasan, Ben Mildenhall, Jonathan T Barron, and Paul Debevec. 2021. Baking neural radiance fields for real-time view synthesis. In *Proceedings of the IEEE/CVF International Conference on Computer Vision*. 5875–5884.
- Ajay Jain, Matthew Tancik, and Pieter Abbeel. 2021. Putting nerf on a diet: Semantically consistent few-shot view synthesis. In *Proceedings of the IEEE/CVF International Conference on Computer Vision*. 5885–5894.
- Nima Khademi Kalantari, Ting-Chun Wang, and Ravi Ramamoorthi. 2016. Learning-based view synthesis for light field cameras. *ACM Transactions on Graphics (TOG)* 35, 6 (2016), 1–10.
- Johannes Kopf, Kevin Matzen, Suhil Alsison, Ocean Quigley, Francis Ge, Yangming Chong, Josh Patterson, Jan-Michael Frahm, Shu Wu, Matthew Yu, et al. 2020. One shot 3d photography. *ACM Transactions on Graphics (TOG)* 39, 4 (2020), 76–1.
- Brooke Krajancich, Petr Kellnhofer, and Gordon Wetzstein. 2020. Optimizing Depth Perception in Virtual and Augmented Reality through Gaze-Contingent Stereo

- Rendering. *ACM Trans. Graph.* 39, 6, Article 269 (nov 2020), 10 pages.
- Marc Levoy and Pat Hanrahan. 1996. Light field rendering. In *Proceedings of the 23rd annual conference on Computer graphics and interactive techniques*. 31–42.
- Lahav Lipson, Zachary Teed, and Jia Deng. 2021. Raft-stereo: Multilevel recurrent field transforms for stereo matching. *arXiv preprint arXiv:2109.07547* (2021).
- Guilin Liu, Fitsum A Reda, Kevin J Shih, Ting-Chun Wang, Andrew Tao, and Bryan Catanzaro. 2018. Image inpainting for irregular holes using partial convolutions. In *Proceedings of the European Conference on Computer Vision (ECCV)*. 85–100.
- Lingjie Liu, Jiatao Gu, Kyaw Zaw Lin, Tat-Seng Chua, and Christian Theobalt. 2020. Neural sparse voxel fields. *arXiv preprint arXiv:2007.11571* (2020).
- Andrew Maimone and Junren Wang. 2020. Holographic Optics for Thin and Light-weight Virtual Reality. *ACM Trans. Graph.* 39, 4, Article 67 (jul 2020), 14 pages.
- Ricardo Martin-Brualla, Rohit Pandey, Shuoran Yang, Pavel Pidlypenskyi, Jonathan Taylor, Julien Valentin, Sameh Khamis, Philip Davidson, Anastasia Tkach, Peter Lincoln, et al. 2018. LookinGood: enhancing performance capture with real-time neural re-rendering. *ACM Transactions on Graphics (TOG)* 37, 6 (2018), 1–14.
- Ben Mildenhall, Pratul P Srinivasan, Rodrigo Ortiz-Cayon, Nima Khademi Kalantari, Ravi Ramamoorthi, Ren Ng, and Abhishek Kar. 2019. Local light field fusion: Practical view synthesis with prescriptive sampling guidelines. *ACM Transactions on Graphics (TOG)* 38, 4 (2019), 1–14.
- Ben Mildenhall, Pratul P Srinivasan, Matthew Tancik, Jonathan T Barron, Ravi Ramamoorthi, and Ren Ng. 2020. Nerf: Representing scenes as neural radiance fields for view synthesis. In *European conference on computer vision*. Springer, 405–421.
- Simon Niklaus and Feng Liu. 2020. Softmax splatting for video frame interpolation. In *Proceedings of the IEEE/CVF Conference on Computer Vision and Pattern Recognition*. 5437–5446.
- Oculus. 2016. *asynchronous spacewarp*. <https://www.oculus.com/blog/introducing-asw-2-point-0-better-accuracy-lower-latency/>
- Albert Pumarola, Enric Corona, Gerard Pons-Moll, and Francesc Moreno-Noguer. 2021. D-nerf: Neural radiance fields for dynamic scenes. In *Proceedings of the IEEE/CVF Conference on Computer Vision and Pattern Recognition*. 10318–10327.
- Christian Reiser, Songyou Peng, Yiyi Liao, and Andreas Geiger. 2021. KiloNeRF: Speeding up Neural Radiance Fields with Thousands of Tiny MLPs. *arXiv preprint arXiv:2103.13744* (2021).
- Jonathan Shade, Steven Gortler, Li-wei He, and Richard Szeliski. 1998. Layered depth images. In *Proceedings of the 25th annual conference on Computer graphics and interactive techniques*. 231–242.
- Meng-Li Shih, Shih-Yang Su, Johannes Kopf, and Jia-Bin Huang. 2020. 3d photography using context-aware layered depth inpainting. In *Proceedings of the IEEE Conference on Computer Vision and Pattern Recognition*. 8028–8038.
- Rajiv Soundararajan and Alan C Bovik. 2012. Video quality assessment by reduced reference spatio-temporal entropic differencing. *IEEE Transactions on Circuits and Systems for Video Technology* 23, 4 (2012), 684–694.
- Pratul P Srinivasan, Richard Tucker, Jonathan T Barron, Ravi Ramamoorthi, Ren Ng, and Noah Snavely. 2019. Pushing the boundaries of view extrapolation with multiplane images. In *Proceedings of the IEEE/CVF Conference on Computer Vision and Pattern Recognition*. 175–184.
- Zhou Wang, Alan C Bovik, Hamid R Sheikh, Eero P Simoncelli, et al. 2004. Image quality assessment: from error visibility to structural similarity. *IEEE Transactions on Image Processing* 13, 4 (2004), 600–612.
- Olivia Wiles, Georgia Gkioxari, Richard Szeliski, and Justin Johnson. 2020. Synsin: End-to-end view synthesis from a single image. In *Proceedings of the IEEE/CVF Conference on Computer Vision and Pattern Recognition*. 7467–7477.
- Lei Xiao, Anton Kaplanyan, Alexander Fix, Matthew Chapman, and Douglas Lanman. 2018. DeepFocus: learned image synthesis for computational displays. *ACM Transactions on Graphics (TOG)* 37, 6 (2018), 1–13.
- Alex Yu, Ruilong Li, Matthew Tancik, Hao Li, Ren Ng, and Angjoo Kanazawa. 2021a. Plenotrees for real-time rendering of neural radiance fields. *arXiv preprint arXiv:2103.14024* (2021).
- Alex Yu, Vickie Ye, Matthew Tancik, and Angjoo Kanazawa. 2021b. pixelnerf: Neural radiance fields from one or few images. In *Proceedings of the IEEE/CVF Conference on Computer Vision and Pattern Recognition*. 4578–4587.
- Kai Zhang, Gernot Riegler, Noah Snavely, and Vladlen Koltun. 2020. Nerf++: Analyzing and improving neural radiance fields. *arXiv preprint arXiv:2010.07492* (2020).
- Tinghui Zhou, Richard Tucker, John Flynn, Graham Fyffe, and Noah Snavely. 2018. Stereo magnification: Learning view synthesis using multiplane images. *arXiv preprint arXiv:1805.09817* (2018).
- C Lawrence Zitnick, Sing Bing Kang, Matthew Uyttendaele, Simon Winder, and Richard Szeliski. 2004. High-quality video view interpolation using a layered representation. *ACM transactions on graphics (TOG)* 23, 3 (2004), 600–608.